

# Object-independent piston diagnosing approach for segmented optical mirrors via deep convolutional neural network

MEI HUI,\* WEIQIAN LI, MING LIU, LIQUAN DONG, LINGQIN KONG, AND YUEJIN ZHAO

Beijing Key Lab. for Precision Optoelectronic Measurement Instrument and Technology, School of Optoelectronics, Beijing Institute of Technology, Beijing 100081, China

\*Corresponding author: huim@bit.edu.cn

Received 8 October 2019; revised 29 November 2019; accepted 13 December 2019; posted 13 December 2019 (Doc. ID 379194); published 17 January 2020

Piston diagnosing approaches based on neural networks have shown great success, while a few methods are heavily dependent on the imaging target of the optical system. In addition, they are inevitably faced with the interference of submirrors. Therefore, a unique object-independent feature image is used to form an original kind of data set. Besides, an extremely deep image-based convolutional neural network (CNN) of 18 layers is constructed. Furthermore, 9600 images are generated as a data set for each submirror with a special measure of sensitive area extracting. The diversity of results among all the submirrors is also analyzed to ensure generalization ability. Finally, the average root mean square error of six submirrors between the real piston values and the predicted values is approximately  $0.0622\lambda$ . Our approach has the following characteristics: (1) the data sets are object-independent and contain more effective details, which behave comparatively better in CNN training; (2) the complex network is deep enough and only a limited number of images are required; (3) the method can be applied to the piston diagnosing of segmented mirror to overcome the difficulty brought by the interference of submirrors. Our method does not require special hardware, and is fast to be used at any time, which may be widely applied in piston diagnosing of segmented mirrors. © 2020 Optical Society of America

<https://doi.org/10.1364/AO.379194>

## 1. INTRODUCTION

Piston sensing is a technique for measuring the piston aberrations of an optical field. So far, several types of piston diagnosing methods have shown great success, including the modified Shack–Hartmann sensors [1], pyramid sensors [2], dispersed fringe sensors [3,4], the interferometry with masks, and diffracting components [5]. However, additional optical components are required, which increase the hardware complexity. Other techniques are able to extract piston errors from the surrounding peaks of modulation transfer functions (MTF), such as the chromatic phase diversity [6], the intersegment piston sensor [7], and calibration retrieval sensing [8,9]. Unfortunately, they are subjected to the size of the object. Phase diversity, an image-based wavefront sensing method, is capable of measuring piston aberrations based on a pair of images captured on the focal and defocused planes [10,11]. Though being of high accuracy, the iterative optimization procedure is usually time-consuming and this method lacks an ample capture range.

Furthermore, a few piston diagnosing methods based on neural networks have been proposed. The back propagation (BP) neural network, a kind of shallow network, was first proposed

to detect wavefront aberrations [12,13]. Then the method for extended objects was developed [14,15]. The traditional BP neural network for piston sensing is very instructive, but it can only work within a narrow spectral band. Hinton devoted himself to addressing the limitation of layers by proposing deep learning [16–18]. Then, the deep network was successfully applied to piston sensing for traditional single-aperture systems [19]. It has been proven that Zernike coefficients can be estimated from point spread function (PSF) through a well-trained convolutional neural network (CNN). And the recent research has demonstrated that piston error can be directly estimated from a single white-light intensity image through CNNs [20].

Piston diagnosing for multiple apertures is different from that for single-aperture systems. Piston sensing is challenged with the phase discontinuity and  $2\pi$  ambiguity. A method of piston alignment for segmented optical mirrors, using defocus images as inputs, has been proven by means of simulations [21]. This method eliminates the requirement of focus diversity and achieves a large capture range, while the network is not deep enough and requires a large number of data sets. Recently, as described in Ref. [22], another method has been successfully

applied to piston sensing for segmented mirrors. The network they used is deep enough to work in an end-to-end mode, which means that the raw images don't have to be complicatedly preprocessed before being fed to the CNN. However, the prediction accuracy is affected by the number and size of the apertures. An object-independent image-based wavefront sensing approach was proposed lately [23]. They introduced long short-term memory (LSTM) into their work and achieved an ideal result. However, this method has not been tested on segmented apertures yet. Therefore, deep network and ideal inputs containing more details might be indispensable, to some degree. They benefit CNN training and play an important role in the prediction accuracy.

In this paper, it is of great significance that a new kind of data set is proposed to contribute to CNN training. These kinds of data sets change regularly, contain more details, and are independent of the imaging target of the optical system. The sensitive areas are also extracted from the feature images to eliminate the distinctive influence brought by the interference of submirrors. Besides, rather than using a shallow network, an extremely deep CNN network of 18 layers is constructed for piston diagnosing from special feature images. The inherent relations between the intensities of the feature images can be recognized and utilized through our network. Furthermore, simulations are performed to demonstrate the effectiveness and accuracy of our method and ensure that it can be successfully applied to the piston alignment of segmented mirrors. Finally, some discussions are also presented to analyze the difference of results among all the submirrors. This will help us generate more appropriate data sets to improve the accuracy in the future.

This paper discusses these aspects. Section 2 gives the theory of simulation. Section 3 gives the method of data-set establishment and the details of the network. Section 4 presents the results of our method. Section 5 summarizes the conclusions.

## 2. THEORY

### A. Adaptive Mirrors

We refer to the primary mirror structure of the Keck telescope [24] and the primary mirror consists of six hexagonal submirrors. The six submirrors are arranged from head to tail, forming a ring. The middle of the structure is a light-passing hole. For convenience of description, a coordinate system is established and each submirror is numbered in proper order. The optical structure is shown in Fig. 1.

### B. Optical Transfer Functions

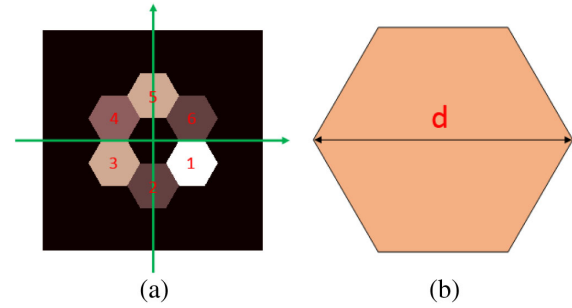
The relations of the focus image captured on the focal plane and the object in the spatial domain in this optical system are

$$i(x, y) = o(x, y) * \text{PSF}(x, y). \quad (1)$$

According to the Fourier optics principle, the relationship in the frequency domain can be written as

$$I(u, v) = O(u, v) \cdot \text{OTF}(u, v). \quad (2)$$

In the above equation,  $i(x, y)$  is the intensity distribution of the image on the ideal focal plane,  $o(x, y)$  is the distribution



**Fig. 1.** (a) Shows the construction of the primary mirror, and (b) shows the dimensions of the segmented sub-aperture.

functions of the two-dimensional object.  $\text{OTF}(u, v)$  is the object transfer function for system.

Aberrations can be expressed as a wavefront  $C(x, y)$  measured in waves, or optical phase  $\varphi(x, y) = 2\pi P(x, y)$  measured in radians. Then, we can write a generalized pupil function  $C(x, y)$  by combining the effects of apodization and aberrations into one complex function

$$C(x, y) = W(x, y) \exp(i2\pi P(x, y)). \quad (3)$$

As shown in Fig. 1, the generalized pupil function of the segmented primary mirror can be written as

$$C(x, y) = \sum_{j=1}^N W_j(x, y) \exp(2\pi i \varphi_j). \quad (4)$$

$W_j$  is the shape function of the submirror and can be given by

$$W_j = \begin{cases} 1 & \text{inside the } j\text{th hexagon} \\ 0 & \text{outside the } j\text{th hexagon.} \end{cases} \quad (5)$$

$\varphi_j$  is the aberration corresponding to the  $j$ th submirror and can be expressed as a linear combination of Zernike polynomials. Only when considering the piston aberration of each submirror,  $\varphi_j$  can be written as

$$\varphi_j = \frac{1}{\lambda} (a_{j1} Z_{j1}). \quad (6)$$

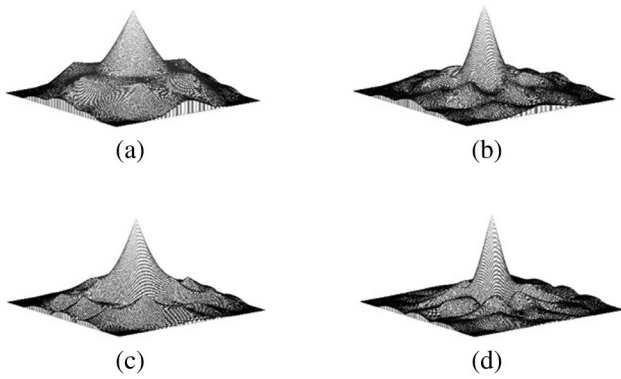
In the above equation,  $Z_{j1}$  is the piston error of the  $j$ th submirror along the optical axis, and  $a_{j1}$  is the corresponding aberration coefficient. The generalized pupil function of the segmented primary mirror can be written as

$$C(x, y) = \sum_{j=1}^N W_j(x, y) \exp\left[i \frac{2\pi}{\lambda} (a_{j1} Z_{j1})\right]. \quad (7)$$

Moreover, the point spread function of the optical system corresponding to the intensity distribution of an ideal focal plane image can be acquired by the inverse Fourier transform of a generalized pupil function:

$$\text{PSF}(u, v) = |\text{FT}^-(C(x, y))|^2. \quad (8)$$

In the above equation,  $\text{FT}^-$  is a two-dimensional inverse Fourier transform operation.



**Fig. 2.** (a) OTF for systems without a piston error and defocus amount. (b) OTF for systems with a defocus amount. (c) OTF for systems with a piston error. (d) OTF for systems with a piston error and defocus amount.

In the same way, the relations of the defocus image captured on the defocused plane and the object in the spatial domain in this optical system are

$$i_{\text{defocus}}(x, y) = o(x, y) * \text{PSF}_{\text{defocus}}(x, y). \quad (9)$$

According to the Fourier optics principle, the relationship in the frequency domain can be written as

$$I_{\text{defocus}}(u, v) = O(u, v) \cdot \text{OTF}_{\text{defocus}}(u, v). \quad (10)$$

The generalized pupil function of the segmented primary mirror can be written as

$$C_{\text{defocus}}(x, y) = A(x, y) \times \exp \{2\pi i [\varphi(x, y) + \varphi_{\text{defocus}}(x, y)]\}. \quad (11)$$

In the above equation,  $\varphi_{\text{defocus}}(x, y)$  is the known defocus amount introduced, represented by the fourth term representing the defocus amount in the Zernike polynomial:

$$\varphi_{\text{defocus}}(x, y) = a_4 c_4(\rho, \theta). \quad (12)$$

In addition,  $\text{PSF}_{\text{defocus}}(u, v)$  can be acquired by the inverse Fourier transform of a generalized pupil function:

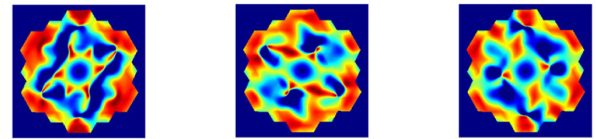
$$\text{PSF}_{\text{defocus}}(u, v) = |\text{FT}^{-1}(C_{\text{defocus}}(x, y))|^2. \quad (13)$$

The OTF images of the simulation process are shown in Fig. 2.

### C. Power Metric

Here, the CNN training set is constructed by the in-focus image and the defocus image of the segmented optics simulation system, which is not related to the imaging content:

$$M_{\text{power}} = \frac{F^* F - D^* D}{F^* F + D^* D}. \quad (14)$$



**Fig. 3.** Some of the simulation for the power metric.

**Table 1.** In-Focus Image and the Defocus Image Formed by the Segmented Mirror Optical System for Different Targets and the Extracted Features for Different Targets with the Same Piston Errors

	Image Target	Grey Image	In-focus Image	Defocus Image	Power Metric	Colored PM
Target1						
Target2						
Target3						
Target4						

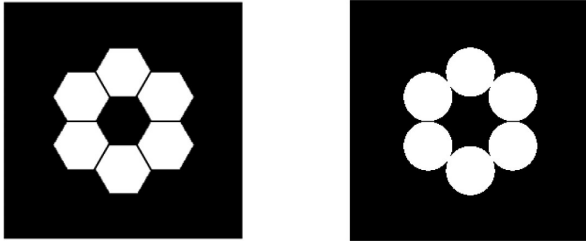


Fig. 4. Segmented mirrors of two shapes.

Table 2. Simulation Parameters

Parameter	Value
Diameter of the primary mirror	$D = 4$ m
Diameter of the submirror	$d = 1.46$ m
Focus length	$l = 40$ m
Defocus length	$L = 400\lambda$
Wavelength	$\lambda = 700$ nm

In the above equation,  $F$  and  $D$  refer to the Fourier spectra of the in-focus and defocus images, respectively.  $M_{\text{power}}$  is the power metric feature quantity represented by the in-focus image and the defocus image [25]. Compared to other kinds of images,  $M_{\text{power}}$  changes regularly and contains more details. Different imaging targets will constitute same data sets as Fig. 3.

Table 1 is the in-focus image and the defocus image formed by the segmented mirror optical system for different targets and the corresponding power metric feature quantity. It can be seen that this feature vector is independent of the imaging content.

We calculate  $M_{\text{power}}$  on segmented mirrors of different shapes. The results are so similar that only one of them is used in our experiments. The structures are shown in Fig. 4.

### D. Parameters of the Imaging System

The relevant parameters of the segmented optics simulation system are listed in Table 2. The primary mirror consists of six hexagon submirrors; the effective apertures of the primary mirror  $D$  and submirror  $d$  are 4 m and 1.46 m, respectively; the focal length is 40 m. The number of waves of quadratic diversity at the edge of the entire six-segment aperture is given by

$$\text{Number of waves of defocus} = \frac{\Delta z}{8\lambda(f\#)^2}. \quad (15)$$

In the above equation,  $f\#$  represents the  $f$  number (focal length/diameter ratio) of the system. The linear distance that the defocused or diverse focal plane must be displaced for 0.5 waves of focus error is given by

$$\Delta z = 4\lambda(f\#)^2. \quad (16)$$

The defocused length is set to  $400\lambda$ .

## 3. METHOD

### A. Generation of Data Sets

In this paper, the segmented mirror has a total of six submirrors. We assume the tip-tilt has been correctly restored previously. A network has been used to solve the ambiguity of  $2\pi$  in the measurement of piston diagnosing [26]. We suppose that the piston errors of all the submirrors are already corrected to  $(0, \lambda)$ . Then,

Table 3. Typical Training Samples and the Training Data Points Used for Each Submirror

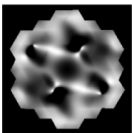
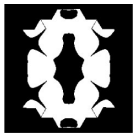
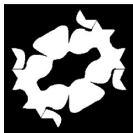

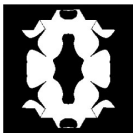
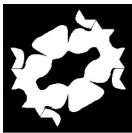
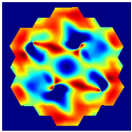
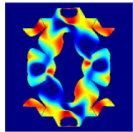
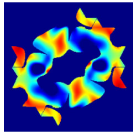
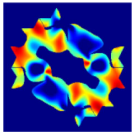
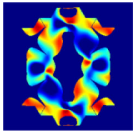
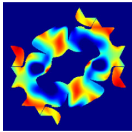
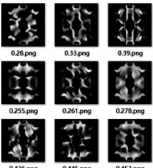
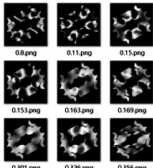
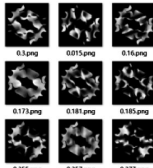
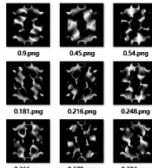
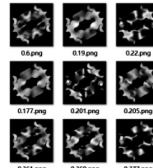
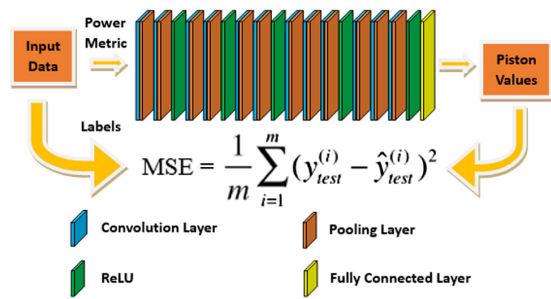
Power Metric	Submirror 2	Submirror 3	Submirror 4	Submirror 5	Submirror 6
					
					

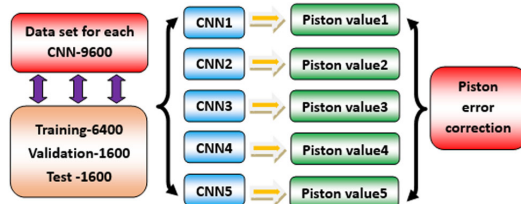
Table 4. Some of the Simulation Images and Labels for the Input of the Network, which are a Part of Simulation Data Set

Submirror 2	Submirror 3	Submirror 4	Submirror 5	Submirror 6
 0.29 μm, 0.33 μm, 0.39 μm 0.25 μm, 0.26 μm, 0.27 μm 0.43 μm, 0.44 μm, 0.45 μm	 0.8 μm, 0.11 μm, 0.15 μm 0.153 μm, 0.163 μm, 0.168 μm 0.307 μm, 0.326 μm, 0.356 μm	 0.3 μm, 0.015 μm, 0.16 μm 0.173 μm, 0.181 μm, 0.185 μm 0.255 μm, 0.357 μm, 0.377 μm	 0.3 μm, 0.45 μm, 0.54 μm 0.181 μm, 0.216 μm, 0.246 μm 0.366 μm, 0.376 μm, 0.383 μm	 0.8 μm, 0.19 μm, 0.22 μm 0.177 μm, 0.201 μm, 0.205 μm 0.361 μm, 0.369 μm, 0.377 μm





**Fig. 5.** Schematic representation of the network architecture.



**Fig. 6.** Prediction flow of the submirror piston error.

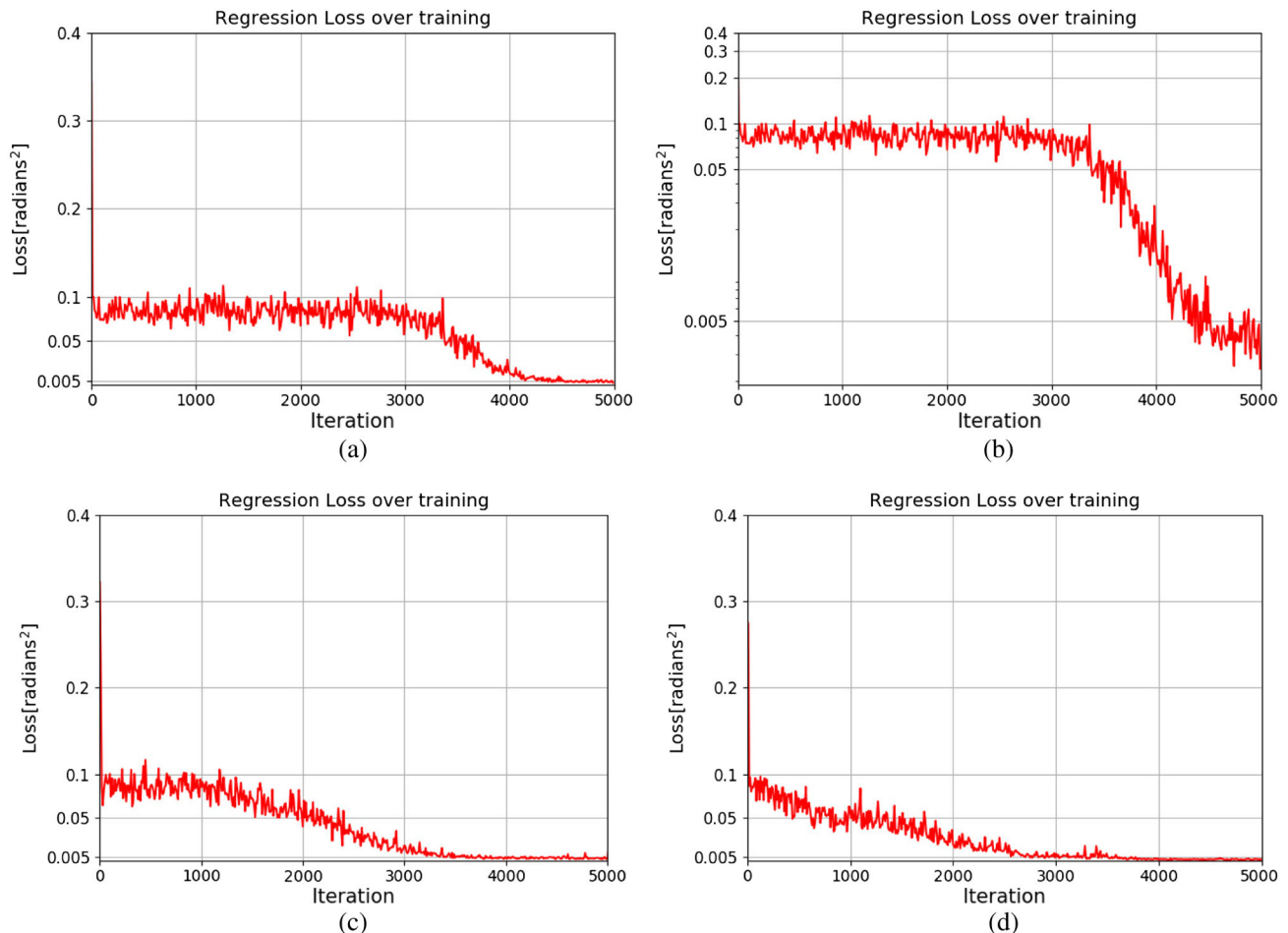
we can identify the piston error of the submirrors between  $(0, \lambda)$  through five CNNs.

We want to build more general data sets that directly predict the error of each submirror. So we use the first submirror as a benchmark. Piston values are selected randomly for the other five segments between  $(0, \lambda)$ . Each data set consists of 6400 training samples, 1600 validation samples, and 1600 test samples. Each sample is labeled by the piston error.

The piston errors of the submirrors interfere with each other, therefore having a bad influence on CNN training. So we also use statistical methods to find the data points in the samples that are sensitive to the piston error of each submirror, which is helpful for the training process. Below we present the data points for every submirror used in the data sets. After many tests, we find that the data sets with sensitive point extraction behave better in the training results than the unprocessed data sets. See Tables 3 and 4 for details.

## B. Network

The network topology was inspired by Visual Geometry Group (VGG) [27]. We compared the performance of four types of VGGs with different number of layers to select the most



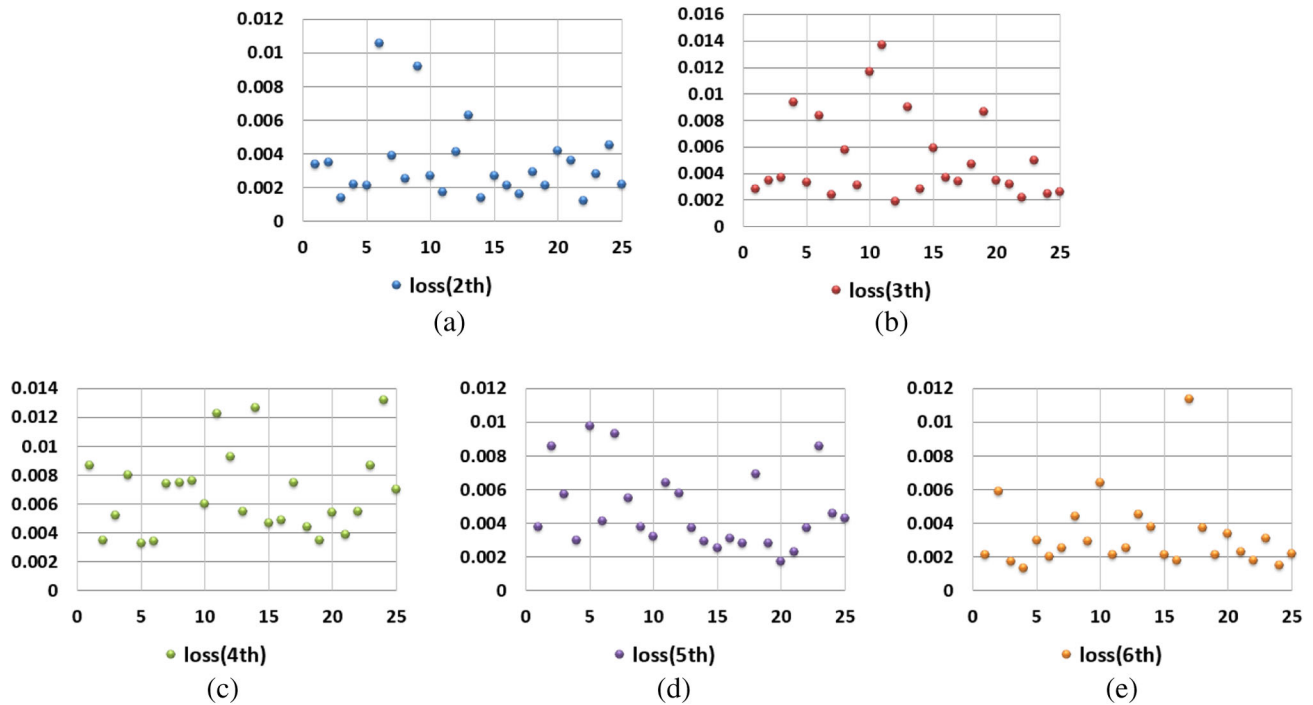
**Fig. 7.** (a) and (b) Regression loss over training in ordinary scale and logarithmic scale for the fourth submirror. (c) and (d) Regression loss over training in ordinary scale for the third and sixth submirrors.

appropriate network that is not only time-saving, but also of high accuracy. We also split the network into five branches with the same loss functions for each. A schematic representation is shown in Fig. 5.

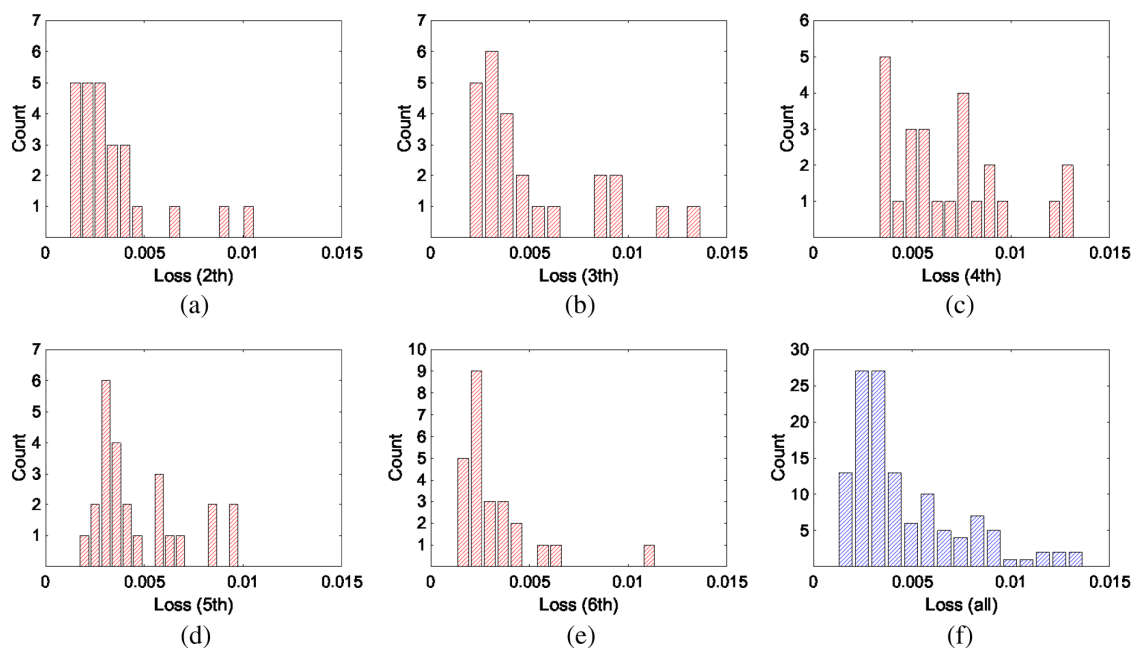
We trained five CNNs with the same structure for identifying piston error of each submirror, except the error of the first submirror. The prediction flow of the algorithm is shown in Fig. 6.

One branch has 12 convolutional layers with rectified linear unit (ReLU) activations, five pooling layers, and a fully connected layer at the end. This is used to predict the piston step

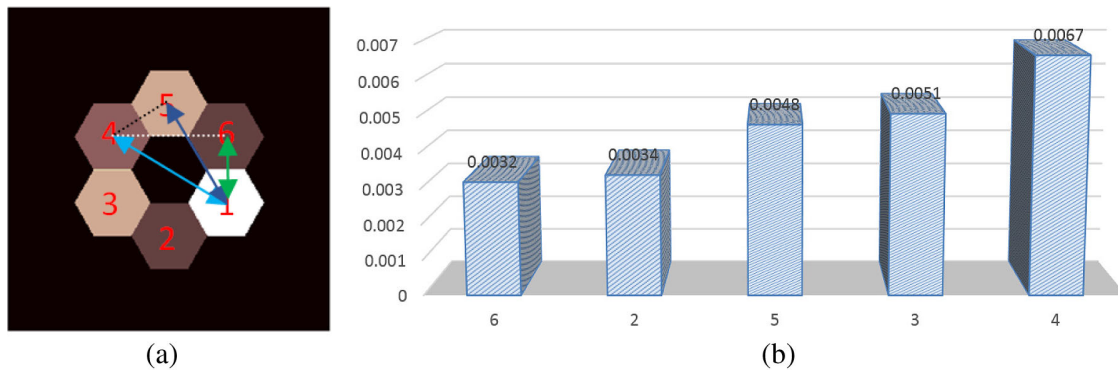
values in the range  $(0, \lambda)$ . The branch is in charge of performing a regression task to predict a continuous value. The cost function in this branch is the mean squared error between the output scores of the last fully connected layer and the ground truth labels or, equivalently, the L2 norm of the difference between the predicted scores and labels. This prediction can be carried out for the information contained in one single wavelength. The CNN is trained in a fully supervised manner, so the input images and labels must be supplied in the process.



**Fig. 8.** MSE of 25 batches from the testing sets of the submirrors from (a) to (e).



**Fig. 9.** Distribution of MSE for test set of each submirror from (a) to (e). (f) shows the distribution of MSE for all the test sets.



**Fig. 10.** (a) Shows the relationship of distance between submirrors. The three arrows represent the different distance from the first submirror to the  $n$ th submirror. Light blue means the furthest distance. Green indicates the closest distance. The distance of dark blue is in the middle. The submirrors with the same color have the same distance. (b) shows the loss of five submirrors respectively. As can be seen from the figure, the loss increases with distance.

We use TensorFlow to build the framework of the CNN. The network parameters are updated with a mini-batch gradient descent algorithm and the Adam update rule [28]. The size of the batch is 64, the number of the learning rate is 0.0001, and the maximum number of iterations is 5000.

#### 4. RESULTS

The training and testing results of the five submirrors are presented and analyzed in this chapter. In the sixth submirror, for example, we can see the evolution of the regression loss over the course of the training in Fig. 7. The vertical axis represents the mean squared error between the predicted piston steps and the ground truth labels. As can be seen from Fig. 7, the loss has a significant decrease and eventually stabilizes at lower values, achieving ideal training results. The loss function of the sixth submirror is similar to that of the second submirror. And the third submirror has almost the same loss function like the fifth submirror, too. So we only show the loss function for three submirrors in figure. Although the rates of decline are different, all five training sets achieve good training results through the CNNs.

Then, we test the well-trained models on the test sets. We have five models corresponding to five submirrors. Test sets and training sets do not contain the same samples. The five test sets are acquired in the same way as the training sets. Each test set has 1600 samples and consists of 25 batches. Besides, the GPU of GTX 1080Ti is used in this process and the test time of each batch is less than 1 s. We perform the cross-correlation test to validate the performance. The Pearson Correlation Coefficients for all five test sets are above 0.9, which represents the predicted value, and the actual values are highly correlated.

The following Fig. 8 shows the results of each batch for the test set among all the submirrors. The test loss from the second submirror to the sixth submirror are 0.0034, 0.0051, 0.0067, 0.0048, and 0.0032. Namely, the RMS errors between the predicted values and real inputs of testing samples are about  $0.0583\lambda$ ,  $0.0714\lambda$ ,  $0.0819\lambda$ ,  $0.0693\lambda$ , and  $0.0566\lambda$ , respectively. The loss of the test set is a little bit higher than that of the training set. However, it's within the reasonable range, which means that the trained model has sufficient generalization

ability. The distributions of loss among the five submirrors are also presented. Each test set has 25 batches and there are a total of 125 batches. As can be seen from the Fig. 9, except for the fourth submirror, most of the losses among 25 batches are below 0.0051 for the other submirrors. And most of the loss among 25 batches are below 0.0068 for the fourth submirror. See Fig. 9 for details.

In the end, the special situation of the fourth submirror is also analyzed. We tried different submirrors as benchmarks, and a special rule was found after many tests. When the distance between the first submirror and the other submirror becomes farther, the loss of test sets gets larger, too. Take the above test results, for example; the loss of the sixth submirror (0.0032) and the second submirror (0.0034) are almost the same. It's about 2 times the number of 0.0017. And the loss of the fifth (0.0048) submirror and the third submirror (0.0051) is about 3 times the number of 0.0017, which is obviously larger. As for the fifth submirror (0.0067), it's approximately 4 times the number of 0.0017, which is the largest. The difference among them is shown in Fig. 10 clearly. If we take one submirror as the benchmark, training and testing on the adjacent submirrors might yield better results.

#### 5. CONCLUSION

In this paper, we propose an object-independent piston diagnosing approach for segmented optical mirrors via a deep CNN. We first construct the new kind of data set and train five image-based CNNs. Then, this method is applied to the piston diagnosing of segmented mirrors. The average root mean square error of the six submirrors between the real piston value and the predicted value is approximately  $0.0622\lambda$ . Most of the batch losses from the test sets are within the range from 0.0017 to 0.0068. Nearly half of the batch losses are within the scope between 0.0017 and 0.0034. The extraction of the object-independent feature image eliminates the interference of the unknown object on image-based piston sensing. Besides, the feature images change regularly and contain more details, which attach great importance to achieving ideal results. Furthermore, a measure of extracting sensitive area is also introduced to eliminate the difficulty brought by the interference of the submirrors. Since

the training process is performed without a large number of data sets, our approach is much easier to implement. The difference of the results among five submirrors is also analyzed, which has prevalent meaning of guidance for us to choose the benchmark when generating data sets in actual alignment. Therefore, the piston diagnosing approach proposed in this paper is more convenient for application and generalization.

Tip-tilt and other sources of errors will be added, and the method should be tested to be robust to the image noise. Besides, we might adjust the data sets and optimize the training results by setting different submirrors as the benchmark, especially the adjacent submirrors. Moreover, our approaches will be introduced into different shapes and numbers of apertures. We will explore these problems further in future work.

**Funding.** National Natural Science Foundation of China (61475018).

**Disclosures.** The authors declare no conflicts of interest.

## REFERENCES

- G. Chanan, M. Troy, F. Dekens, S. Michaels, J. Nelson, T. Mast, and D. Kirkman, "Phasing the mirror segments of the Keck telescopes: the broadband phasing algorithm," *Appl. Opt.* **37**, 140–155 (1998).
- S. Esposito, E. Pinna, A. Puglisi, A. Tozzi, and P. Stefanini, "Pyramid sensor for segmented mirror alignment," *Opt. Lett.* **30**, 2572–2574 (2005).
- M. A. van Dam, B. A. McLeod, and A. H. Bouchez, "Dispersed fringe sensor for the Giant Magellan Telescope," *Appl. Opt.* **55**, 539–547 (2016).
- F. Shi, D. C. Redding, A. E. Lowman, C. W. Bowers, L. A. Burns, P. Petrone, III, C. M. Ohara, and S. A. Basinger, "Segmented mirror coarse phasing with a dispersed fringe sensor: experiment on NGST's wavefront control testbed," *Proc. SPIE* **4850**, 31–328 (2003).
- M. Deprez, C. Bellanger, L. Lombard, B. Wattellier, and J. Primot, "Piston and tilt interferometry for segmented wavefront sensing," *Opt. Lett.* **41**, 1078–1081 (2016).
- D. Mourard, W. Dali Ali, A. Meilland, N. Tarmoul, F. Patru, J. M. Clausse, P. Girard, F. Henault, A. Marcotto, and N. Mauciert, "Group and phase delay sensing for cophasing large optical arrays," *Mon. Not. R. Astron. Soc.* **445**, 2082–2092 (2014).
- J. F. Simar, Y. Stockman, and J. Surdej, "Single-wavelength coarse phasing in segmented telescopes," *Appl. Opt.* **54**, 1118–1123 (2015).
- J. Jiang and W. Zhao, "Phasing piston error in segmented telescopes," *Opt. Express* **24**, 19123–19137 (2016).
- W. Zhao and Q. Zeng, "Simultaneous multi-piston measurement method in segmented telescopes," *Opt. Express* **25**, 24540–24552 (2017).
- R. L. Kendrick, J.-N. Aubrun, R. Bell, R. Benson, L. Benson, D. Brace, J. Breakwell, L. Burriesci, E. Byler, J. Camp, G. Cross, P. Cuneo, P. Dean, R. Digumerthi, A. Duncan, J. Farley, A. Green, H. H. Hamilton, B. Herman, K. Lauraitis, E. de Leon, K. Lorell, R. Martin, K. Matosian, T. Muench, M. Ni, A. Palmer, D. Roseman, S. Russell, P. Schweiger, R. Sigler, J. Smith, R. Stone, D. Stubbs, G. Swietek, J. Thatcher, C. Tischhauser, H. Wong, V. Zarifis, K. Gleichman, and R. Paxman, "Wide-field Fizeau imaging telescope: experimental results," *Appl. Opt.* **45**, 4235–4240 (2006).
- R. G. Paxman and J. R. Fienup, "Optical misalignment sensing and image reconstruction using phase diversity," *J. Opt. Soc. Am. A* **5**, 914–923 (1988).
- J. R. P. Angel, P. Wizinowich, M. Lloyd-Hart, and D. Sandler, "Adaptive optics for array telescopes using neural-network techniques," *Nature* **348**, 221–224 (1990).
- P. L. Wizinowich, M. Lloydhart, B. A. McLeod, D. Colucci, R. G. Dekany, D. M. Wittman, J. R. P. Angel, D. W. McCarthy, W. G. Hulburd, and D. G. Sandler, "Neural network adaptive optics for the multiple-mirror telescope," *Proc. SPIE* **1542**, 148–158 (1991).
- R. L. Kendrick, D. S. Acton, and A. L. Duncan, "Phase-diversity wavefront sensor for imaging systems," *Appl. Opt.* **33**, 6533–6546 (1994).
- H. Yi, Y. Li, C. Fan, and J. Wang, "A new method of phase diversity wave-front sensing based on SOFM NN," *Guangzi Xuebao* **7**, 352–354 (2008).
- G. E. Hinton, "Deep belief networks," *Scholarpedia* **4**, 5947 (2006).
- M. T. McCann, E. Froustey, M. Unser, and K. H. Jin, "Deep convolutional neural network for inverse problems in imaging," *IEEE Trans. Image Process.* **26**, 4509–4522 (2017).
- R. K. Olga, J. Deng, H. Su, J. Krause, S. Satheesh, S. Ma, Z. Huang, A. Khosla, K. Aditya, M. Bernstein, A. C. Berg, and F. Li, "ImageNet large scale visual recognition challenge," *Int. J. Comput. Vis.* **115**, 211–252 (2014).
- S. W. Paine and J. R. Fienup, "Machine learning for improved image-based wavefront sensing," *Opt. Lett.* **43**, 1235–1238 (2018).
- Y. Nishizaki, M. Valdivia, R. Horisaki, K. Kitaguchi, M. Saito, J. Tanida, and E. Vera, "Deep learning wavefront sensing," *Opt. Express* **27**, 240–251 (2019).
- D. Guerra-Ramos, L. Díaz-García, J. Trujillo-Sevilla, and J. M. Rodríguez-Ramos, "Piston alignment of segmented optical mirrors via convolutional neural networks," *Opt. Lett.* **43**, 4264–4267 (2018).
- X. Ma, Z. Xie, H. Ma, Y. Xu, G. Ren, and Y. Liu, "Piston sensing of sparse aperture systems with a single broadband image via deep learning," *Opt. Express* **27**, 16058–16070 (2019).
- Q. Xin, G. Ju, C. Zhang, and S. Xu, "Object-independent image-based wavefront sensing approach using phase diversity images and deep learning," *Opt. Express* **27**, 26102–26119 (2019).
- G. Chanan, C. Ohara, and M. Troy, "Phasing the mirror segments of the Keck telescopes II: the narrow-band phasing algorithm," *Appl. Opt.* **39**, 4706 (2000).
- R. L. Kendrick, D. S. Acton, and A. L. Duncan, "Phase-diversity wavefront sensor for imaging systems," *Appl. Opt.* **33**, 6533 (1994).
- D. Li, S. Xu, D. Wang, and D. Yan, "Large-scale piston error detection technology for segmented optical mirrors via convolutional neural networks," *Opt. Lett.* **44**, 1170–1173 (2019).
- K. Simonyan and A. Zisserman, "Very deep convolutional networks for large-scale image recognition," arXiv:1409.1556 (2014).
- D. P. Kingma and J. Ba, "Adam: a method for stochastic optimization," arXiv:1412.6980 (2014).